Journal of Materials Research and Technology 30 (2024) 473–484

Contents lists available at ScienceDirect

Journal of Materials Research and Technology

journal homepage: www.elsevier.com/locate/jmrt

Enhancement of mechanical and physical properties of Cu–Ni composites by various contents of Y_2O_3 reinforcement

Walaa Abd-Elaziem [a], Atef Hamada [b], Tarek Allam [c,*,1], Moustafa M. Mohammed [d], Mohammad Abd-El Hamid [a], Sally Samah [a], Doaa Wasfy [a], Moustafa A. Darwish [e], Y Omayma Abd Elguad El-Kady [f], Sally Elkatatny [g]

[a] Department of Mechanical Design and Production Engineering, Faculty of Engineering, Zagazig University, 44519, Egypt
[b] Kerttu Saalasti Institute, Future Manufacturing Technologies (FMT), University of Oulu, Pajatie 5, FI-85500, Nivala, Finland
[c] Institute of Energy and Climate Research: Structure and Function of Materials (IEK-2), Forschungszentrum Jülich GmbH, 52425, Jülich, Germany
[d] Mechanical Department, Faculty of Technology and Education, Beni-Suef University, Beni Suef, 62511, Egypt
[e] Physics Department, Faculty of Science, Tanta University, Tanta, 31527, Egypt
[f] Powder Technology Division, Manufacturing Technology Department, Central Metallurgical R&D Institute, P.O. 87, Helwan, Cairo, 11421, Egypt
[g] Mechanical Engineering Department, Faculty of Engineering, Suez Canal University, Ismailia, 41522, Egypt

ARTICLE INFO

Keywords:
Cu-matrix composites
Cu–Ni
Powder metallurgy
Yttria
Mechanical properties
Coefficient of thermal expansion

ABSTRACT

The increasing demand for materials possessing enhanced mechanical strength, high thermal conductivity, and excellent electrical properties has grown significantly. Cu-matrix composites, especially Cu– Ni, present a promising candidate to fulfill these demands. In this study, Cu–Ni composites were successfully synthesized using powder metallurgy with various additions (0–1.5 wt%) of Yttria (Y_2O_3)-reinforcement aiming to enhance their mechanical, thermal, and electrical properties. The microstructural investigations demonstrated a uniform distribution of Y_2O_3 particles and a slight increase in porosity of the Cu–Ni matrix. The Cu–Ni composites with 1.5 wt% Y_2O_3 showed the presence of Cu_2NiZn intermetallic compounds, potentially harming their physical and mechanical properties. Y_2O_3-reinforcement significantly increased the hardness and led to a moderate rise in the yield and ultimate compressive strengths. The results indicated that the Cu–Ni matrix without Y_2O_3-reinforcement had the highest coefficient of thermal expansion, which decreased with the addition of Y_2O_3, potentially leading to improved thermal properties of Cu–Ni composites. This study puts an emphasis on the importance of Y2O3 particles dispersion and on the extent of porosity in enhancing the thermal and mechanical properties of Cu–Ni composites.

1. Introduction

High thermal conductivity materials are vital for electronic devices, heat sinks, and turbines operating in high-temperature environments [1,2]. Cu is favored for its superior thermal and electrical conductivity, making it an optimal choice for effective heat spreaders and sinks, despite challenges when used with semiconductors due to differences in thermal expansion coefficients [3–6].

However, the drawbacks of Cu, such as creep and reduced strength at high temperatures [7], are addressed by designing particle-reinforced Cu, particularly dispersion-strengthened Cu with less than 5 vol% of reinforcing particles [8,9]. This approach aims to enhance materials' performance in elevated temperature scenarios [10,11]. The ideal design prerequisites for these materials encompass several factors: an even dispersion of fine particles to ensure resistance against creep and fatigue, chemical and thermodynamic stability at temperatures up to 1300 K to uphold mechanical strength and high thermal conductivity, a minimal gap in coefficients of thermal expansion between the particle and matrix, and the absence of phase transformations for dispersion particles [9]. Oxide dispersion particles, while beneficial, can introduce thermal conduction hindrance through phonon scattering [8]. The key difficulty lies in the careful selection of the most appropriate oxide material.

It was reported that Y_2O_3 is superior due to its physical properties

* Corresponding author.
E-mail address: t.allam@fz-juelich.de (T. Allam).
[1] On an unpaid leave from Department of Metallurgical and Materials Engineering, Suez University, 43528, Suez, Egypt.

https://doi.org/10.1016/j.jmrt.2024.03.075
Received 22 December 2023; Received in revised form 2 March 2024; Accepted 12 March 2024
Available online 16 March 2024

[12] and thermodynamic stability compared to counterparts like Al_2O_3 [13,14] and SiC [15,16]. The incorporation of Ni is used to enhance thermal conductivity to compensate for oxide-related deficits, with the optimal composition displaying heightened conductivity and hardness through contribution of Ni [17].

The cold plate technique, employing a porous structure, stands out as an efficient approach for dissipating heat in electronic devices, leveraging the porous media's capacity to raise the contact surface area with the coolant and improve the mixing of fluid flow, thereby enhancing convective heat transfer between porous matrix and fluid [18]. Powder Metallurgy [P/M] is commonly employed to fabricate electronics components, meeting performance requirements effectively [19]. This method proves more competitive than alternatives like casting, stamping, or machining, especially when demanding attributes like strength, wear resistance, or high operating temperatures are needed. P/M offers precision, reducing the need for extensive finishing machining operations required in casting [20,21]. In the pursuit of enhancing the mechanical bond between the Cu matrix and Y_2O_3, a key consideration involves coating ceramics with Cu.

Joshi et al. [22] employed in-situ chemical reduction and high-energy milling techniques to create Cu–Y_2O_3 nanocomposites with two distinct morphologies. Findings indicated that the nano Cu– Y_2O_3 composite prepared via chemical reduction exhibited superior density (83%) compared to the high-energy ball-milled composite (64%). Additionally, the chemically reduced composite displayed enhanced physical and mechanical properties, resulting in stronger in-situ Cu-matrix reinforcement. Shabadi et al. [4] investigated the influence of Y_2O_3 particle incorporation through friction stir processing on the Coefficient of Thermal Expansion (CTE) and thermal conductivity (TC) of Cu. Their research showed that Cu samples with evenly dispersed Y_2O_3 particles (up to 9 passes) experienced a 27% decrease in CTE compared to pure Cu. Geng et al. [23] developed an advanced Cu-based contact material using PM. They incorporated Y_2O_3 as a dispersion-strengthening phase within the Cu alloy (with an average size of 46 μm). They assessed the impact of smaller Y_2O_3 particles (5 μm in size) on the material's performance. Additionally, B_4C was added for antifriction purposes and Bi was used for arc extinction. The microstructure analysis revealed that while Cu particles maintained a rounded ball shape, Y_2O_3 particles exhibited irregular shapes with cracks and extensive surface areas.

Y_2O_3 significantly affected various parameters, causing structural changes, including lattice distortion and shifts in spectral line diffraction. Y_2O_3 atoms tended to accumulate at grain boundaries, hindering the unrestricted growth of Cu grains and leading to refinement. This effect contributed to a reduction in thermal expansion of Cu. Additionally, they found that hardness increased from 35.5 HB to 42.9 HB with the addition of up to 2.0 wt% Y_2O_3, attributed to fine grain strengthening resulting from the distribution of Y_2O_3 at grain boundaries. However, the presence of Y_2O_3 at grain boundaries also negatively affected conductivity [23].

Stobrawa and Rdzawski [24] fabricated Cu nanoscomposite, through the PM route, and investigated their stability at elevated temperatures by incorporating strengthening ceramic materials like oxide or carbide phases. They reported that the efficiency of nanostructure stabilization depends on these phases' volume fraction and dispersion degree. Additionally, the study demonstrated that increasing Y_2O_3 content up to 2 wt% decreased density due to the existence of Y_2O_3 particles around Cu grain boundaries. The authors concluded that the addition of nano-sized ceramic Y_2O_3 (up to 2%) improved mechanical properties compared to materials with microcrystalline grain sizes. However, this enhancement negatively affected plastic deformation due to the abundance of dislocations and agglomeration.

To achieve the desired balance of TC and CTE, it is imperative to control various parameters, including size, type, volume fraction, and distribution pattern of reinforcements. A wide range of reinforcements, such as diamond particles, graphite in various forms, carbon fibers, carbon nanotubes, SiC, W, Mo, and hybrid Y_2O_3 and WO_3 particles, have been introduced to mitigate a high CTE of Cu.

In the current study, our main goal is to develop Cu–Ni based composites enriched with nano Y_2O_3 particle and achieve a balanced behavior with respect to the thermal conductivity and mechanical strength of Cu–Ni composite by incorporating various Y_2O_3 contents. This goal can be realized by adjusting the dispersion, and content of Y_2O_3 particles embedded within the Cu–Ni matrix. Consequently, our study embarks on a multifaceted exploration, encompassing key facets such as optimized microstructure, thermal efficiency, and mechanical strength.

2. Materials and methods

2.1. Materials

In the context of this research, we employed atomized Cu powder containing trace amounts of brass and Ni powder with a purity of around 99.9% with mean particle sizes of approximately 50 nm as the metal matrix materials. As a ceramic reinforcement for the Cu–Ni matrix, we utilized Y_2O_3 nanoparticles, boasting a remarkable purity of 99.995% and exhibiting a particle size range between 30 and 50 nm. For a comprehensive understanding of the properties of the powders utilized in this study, Table 1 presents a detailed summary encompassing the characteristics of the Cu, Ni, and Y_2O_3 materials.

The used Cu powder was heat treated in a reduction process at 450 °C for 1 h under a hydrogen atmosphere in a s tube furnace to remove the moisture and to reduce oxides residual. Equation (1) succinctly illustrates the chemical reaction that takes place during this reduction process, highlighting the role of hydrogen gas in achieving the reduction of Cu to its desired state. Fig. 1 represents the Cu reduction cycle in the furnace.

$$Cu\,O + H_2 = Cu + H_2O \tag{1}$$

2.2. Milling and compaction process

The milling process was carried out in a PQ-N2 planetary ball mill equipped with four rotary containers, each containing 10 mm tungsten carbide (WC) balls (as depicted in Fig. 2). The milling operation ran at a constant rotational speed of 350 revolutions per minute (rpm) and continued for a duration of 24 h. This extended milling period was essential to ensure the thorough homogenization of the mixture, distribution of particles, and to avoid powder clustering. However, this extended milling periods can increase the risk of contamination. Sources of contamination include wear of milling media and attrition of container walls, potentially introducing impurities into the powder mixture. To mitigate this risk, we tried to keep measures such as regular equipment cleaning, careful selection of milling media and container materials to ensure lower contamination acquired. Periodic sampling and analysis of the milled powder can help monitor contamination levels and ensure product quality throughout the milling process. The composition of the resulting powder mixture for fabricating metal matrix composites (MMCs) comprised Cu, 5 wt% Ni, and varying concentrations of Y_2O_3 (0.5, 1, and 1.5 wt%).

Following the milling process, the next step involved compacting the composite powder specimens. A uniaxial compression machine was

Table 1
Physical properties of Cu, Ni, and Y_2O_3 powders used in the study [25–27].

Powder	Density (g/cm^3)	Thermal conductivity ($W.m^{-1}.K^{-1}$)	Thermal expansion)	Electrical resistivity ($\mu\Omega.cm$)
Cu	8.96	401	16.5	1.673
Ni	8.88	60.7	13.4	6.4
Y_2O_3	5.03	13.6	6–7	–

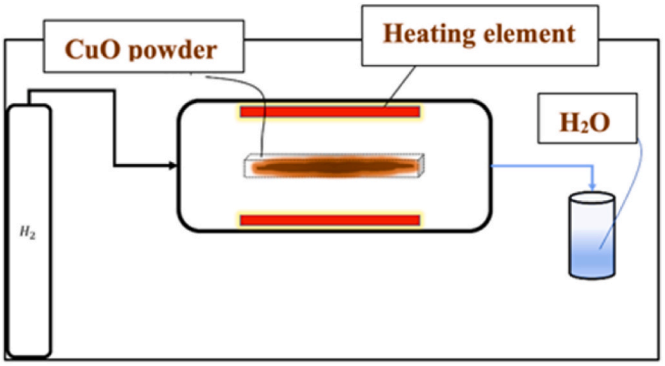

Fig. 1. Cu powder reduction cycle in the high-temperature tube Furnace.

employed for this purpose. The compaction die utilized in this process was constructed from Cr–Mo alloy steel (DIN W302). A pressure of 650 MPa was applied during the cold compaction technique. As a result of this process, compacted specimens with dimensions of 7 mm in height and 8 mm in diameter were obtained.

2.3. Sintering process

The compacted samples were sintered at 950 °C for 90 min under Ar gas. Fig. 3. Represents the heating cycle for composites. Initially, the temperature was elevated from room temperature to 450 °C at a heating rate of 3 °C/min and soaking at this temperature for 25 min to expel any gases embedded in the pores. Subsequently, heating rate of 5 °C/min up to 950 °C, then held at this temperature for 90 min. Finally, the furnace was turned off, and the sintered samples were allowed to cool inside the furnace to protect them from any oxidation effects.

2.4. Microstructure investigations

A comprehensive analysis of the Cu–Ni composites with and without Y_2O_3 was carried out using X-ray diffraction (XRD) and scanning electron microscope (SEM) equipped with an energy-dispersive X-ray spectroscopy (EDS) detector attachment. The composition of phases within the customized composites was analyzed using XRD with a Diffractometer EMPYREAN from PANalytical. This XRD system was equipped with a Bragg Brentano HD mirror (divergence = 0.4°), a 0.02 rad soller slit, and a PIXcel3D detector. Cu-Kα radiation with a wavelength (λ) of 0.15418 nm was employed at an operating voltage of 40 kV and current of 40 mA. The scanning range encompassed 2θ angles from 25 to 100°, with a time per step of 0.5 s and a step size of 0.0131°. For quantitative phase analysis and lattice parameter determination, profile fits were carried out using the Rietveld method. The software employed for this purpose was TOPAS v.6 from Bruker AXS, with crystal structures referenced from the Inorganic Crystal Structure Database (ICSD) (using the up-to-date web version under a campus license). To prepare the sample surfaces for further analysis, a sequence of grinding and polishing techniques was employed. The specimens were initially ground using silicon carbide (SiC) papers with varying grit numbers, extending up to 2000 grit. Following this, mechanical polishing was carried out using a 0.3 μm alumina suspension, which was subsequently followed by chemical polishing using colloidal silica.

To estimate the density of the sintered specimens, the Archimedes rule was applied, conforming to ASTM D1217 standards. Equation (2) and Equation (3) was used for estimating actual densities (ρ_{ac}), and the theoretical densities (ρ_{th}), respectively. Porosity values were determined using Equation (4), with relative density representing the ratio of actual density to theoretical density.

$$\rho_{ac} = \frac{M_a}{(M_a - M_w)} \quad (2)$$

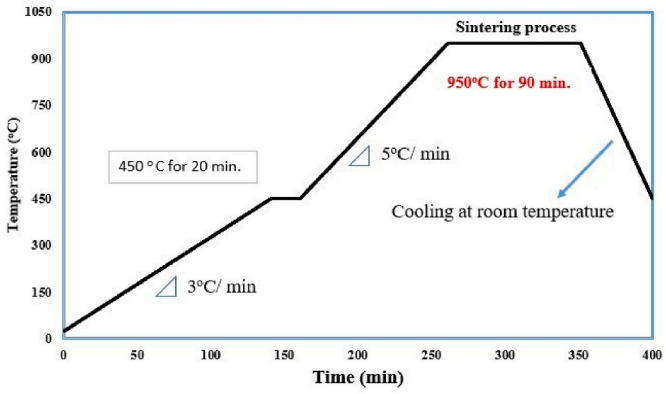

Fig. 3. Thermal cycle during the sintering process carried out in vacuum furnace for Cu–Ni composites reinforced with various Y_2O_3 concentrations.

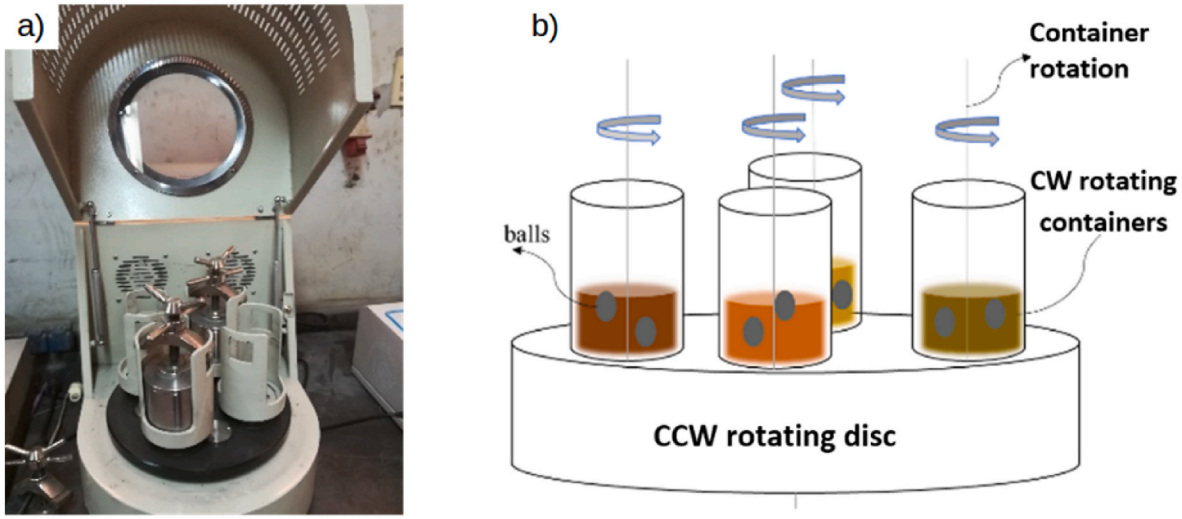

Fig. 2. (a) The planetary ball milling machine used for powder mixing and milling, and (b) a schematic representation of the ball milling process. CW and CCW stand for clockwise and counterclockwise directions, respectively.

$$\frac{1}{\rho_{th}} = (W/\rho_M) + (R/\rho_R) \quad (3)$$

$$Porosity\% = \frac{(\rho_{th} - \rho_{ac})}{\rho_{th}} \quad (4)$$

Where; M_a is the specimen mass in air, M_W is the specimen mass in water, W is the weight fraction of the matrix, R is the weight fraction of reinforcement, ρ_M is the matrix density, ρ_R is the reinforcement density.

2.5. Mechanical characterizations

The mechanical strength of the concerned composites was determined through uniaxial compression tests conducted at room temperature and a strain rate of 1 mm/min using a Lloyd universal testing. The used specimens are of 8 mm in diameter and 7 mm in height. The macro hardness of the Cu–Ni/Y_2O_3 composites was measured using a Vickers's macro-hardness testing apparatus of type HPV 30MPTA. A standard load of 3 kg was applied for a duration of 15 s, and the resulting hardness values were calculated as the average of 15 measurements taken across the examined surfaces.

2.6. Physical characterizations

2.6.1. Electical resistivity

To determine the electrical resistivity of the sintered discs, the four-probe method was employed. A PCE_COM 20 Conductivity Tester (PCE) was utilized for this purpose, and measurements were obtained from three specimens for each Cu–Ni/Y_2O_3 wt.%. Resistivity values ρ (in μ Ω. cm) were calculated using Equation (5), where R represents resistance (in micro-ohms), L is the measured length (in cm), and A signifies the area of cross-section (in cm^2).

$$\rho = \left(\frac{R \times A}{L}\right) \quad (5)$$

Thermal conductivity measurements were derived from electrical resistivity data using the Wiedemann-Franz equation, as expressed in Equation (6). This equation, considering thermal conductivity (λ), electrical conductivity (σ), absolute temperature (T), and the Lorentz number (L), allowed for an accurate determination of thermal conductivity.

$$\lambda = L \times T \times \sigma \quad (6)$$

2.6.2. Coefficient of thermal expansion

The CTE was evaluated by recording measurements over a temperature range of 25 °C–700 °C, with a controlled heating rate of 3 °C per minute. To determine CTE values at specific temperatures, calculations were conducted based on the recorded thermal expansion curves, which provided information on changes in length relative to temperature. This thorough assessment encompassed the heating process from room temperature to 700 °C and was performed in accordance with the formula detailed in Equation (7).

$$CTE = \frac{\partial}{\partial T}\left(\frac{\Delta L}{L}\right) \quad (7)$$

where L is the specimen's original length, and ΔL is the change in length afterward thermal cycling.

3. Results and discussion

3.1. Microstructural features

The XRD patterns of the processed composites containing varying Y_2O_3 contents are illustrated in Fig. 4. In these XRD results, it is evident that the different Cu–Ni composites reinforced with Y_2O_3 exhibit strong peaks corresponding to Cu, as confirmed by reference database ICSD 7954 and shown in Fig. 4 (a). The peaks associated with the oxides, owing to their small fractions and the significant intensity of the Cu peaks, were not clearly discernible. To provide a closer view, a specific angular range of the XRD pattern for the composite with 1.5 wt% Y_2O_3 is presented in Fig. 4b. This view restricts the peak intensity, allowing the tiny peaks to become visible. Notably, visible peaks (shown in blue) correspond to the Y_2O_3 oxide, as per reference database ICSD 34083. Additionally, two peaks (in green) are attributed to Cu_2O oxide. The results of the Rietveld refinement analysis, providing microstructural information about the constituents in the composites, are presented in Table 2.

Fig. 5 presents the SEM micrographs of he initial powders involved in manufacturing the Y_2 O_3 -reinforced Cu–Ni composites. The microstructure of the Cu powder has folded/spread flakes morphology with smooth surfaces (Fig. 5 a). Ni particles have semi-spherical shaped with sharp morphology (Fig. 5 b). However, the Y_2O_3 powders are agglomerated and appear in irregular sharp-edged shapes and larger surface areas as shown in Fig. 5 c. Moreover, the morphology of Cu–Ni-1 wt.% Y_2O_3 raw powders after milling at different magnifications are illustrated in Fig. 6. Particles tend to agglomerate due to the large surface area-to-volume ratio of nanoparticles, which amplifies the van der Waals forces between them.

Fig. 7 shows SEM micrographs of sintered pure Cu–Ni, Cu–Ni/(0.5) Y_2O_3, Cu–Ni/(1) Y_2O_3, and Cu–Ni/(1.5) Y_2O_3. Several pores can be observed in the manufactured composites, as highlighted by the red arrows. The results in Fig. 7b demonstrate that the Y_2O_3 content at 0.5

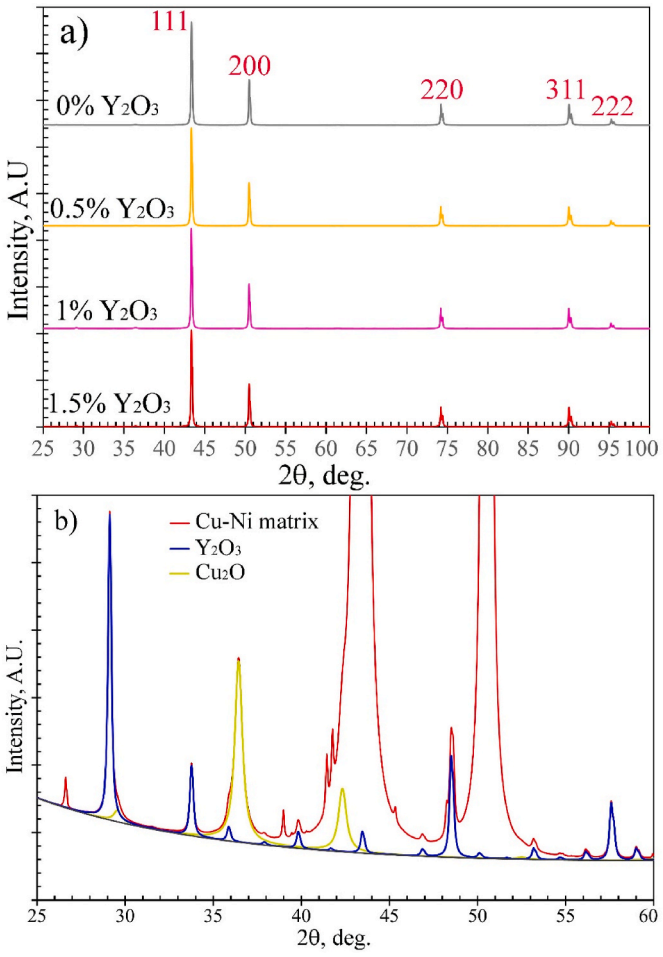

Fig. 4. (a) XRD patterns of Cu–Ni composites reinforced with various Y_2O_3 contents, and (b): enlarged XRD pattern of Cu–Ni composite with 1.5 wt% Y_2O_3, highlighting the invisible oxide peaks in (a).

Table 2
Results of Rietveld refinement analyses for the microstructural information of constituents in the Cu–Ni composites with varying Y_2O_3 contents.

Cu–5%Ni composite	Phase	ICSD	Wt.%	SG	a (Å)
0% Y_2O_3	Cu	7954	99	Fm-3m	3.611
	Cu_2O	172174	1	Pn-3m	4.268
0.5% Y_2O_3	Cu	7954	99	Fm-3m	3.612
	Cu_2O	172174	0.6	Pn-3m	4.268
	Y_2O_3	34083	0.4	Ia-3	10.599
1% Y_2O_3	Cu	7954	96	Fm-3m	3.6125
	Cu_2O	172174	2.8	Pn-3m	4.268
	Y_2O_3	34083	1.2	Ia-3	10.609
1.5% Y_2O_3	Cu	7954	97	Fm-3m	3.612
	Cu_2O	172174	1.5	Pn-3m	4.268
	Y_2O_3	34083	1.5	Ia-3	10.608

wt% exhibits the highest porosity and the lowest densification. This high porosity is due to the poor wettability between the Cu matrix and Y_2O_3 with small percentages. These pores, which have the potential to negatively impact the mechanical properties of the composites, may be attributed to the expulsion of trapped gases during the compact densification process and the limited wetting between the Cu–Ni matrix and the Y_2O_3 reinforcements. In Fig. 7c and d, the microstructure of the samples containing 1 wt% and 1.5 wt% of Y_2O_3 primarily comprises the Cu–Ni matrix with traces of brass.

According to the binary system of the Cu–Ni phase diagram illustrated in Fig. 8, the presence of Ni in the matrix with 5 wt% and 95 wt% of Cu leads to the forming of a solid solution between Cu and Ni of α phase [28]. This occurs due to heat treatment of Cu–Ni prepared by powder metallurgy technique at 950 °C at 5 wt% of Ni. The Y_2O_3 particle addition into the Cu–Ni matrix that comprises trace amount of brass resulted in the appearance of a third phase, specifically the Cu_2NiZn phase. This transformation is evident in the microstructures of samples containing 1.5 wt% Y_2O_3; (Fig. 7d). The Y_2O_3 nanoparticles is considered as a catalyst in promoting the formation of Cu_2NiZn intermetallic compound within the composite. This catalytic effect can be attributed to several mechanisms: (i) Heterogeneous Nucleation: Y_2O_3 nanoparticles act as nucleation sites, providing favorable locations for the initiation of the Cu_2NiZn phase. (ii) Enhanced Atomic Diffusion: At elevated temperatures during processes like sintering, Y_2O_3 can accelerate atomic diffusion along the interfaces between the metal matrix constituents. Nanoparticles can introduce local stress concentrations in the matrix due to differences in thermal expansion coefficients or lattice mismatch. These stresses can promote atomic movement and increase diffusion rates. This increased diffusion facilitates the coming together of Cu, Zn, and Ni atoms, promoting the formation of Cu_2NiZn intermetallic phases. (iii) Oxygen Affinity and Improved Metal Contact: Y_2O_3 exhibits an affinity for oxygen [29], which can help remove oxide layers from the surfaces of metal particles. This removal facilitates direct metal-to-metal contact and fosters interactions between Cu, Zn, and Ni, ultimately leading to the formation of their respective intermetallic compounds.

Fig. 9 also displays high-magnification SEM images of the sintered composites containing Y_2O_3 particles. As shown in Fig. 9, the distribution of Y_2O_3 particles within the Cu matrix is considerably uniform. It's worth noting that having a homogeneous distribution of reinforcements in the sintered composite is crucial for ensuring consistent mechanical properties and an even distribution of stress. This has the added benefit of preventing dislocation movement. Consequently, the interface between the matrix and ceramic particles plays a pivotal role in determining the structure and mechanical characteristics of the composites [30–32]. In general, Cu-metal matrix composites exhibit three types of interface bonding structures: mechanical bonding, diffusion bonding, and chemical bonding, with bonding strength increasing in that order [33,34]. The challenge of achieving good wettability between Cu and Y_2O_3 nanoparticles can be attributed to Cu's stable electron configuration, which includes a full 3d orbital. Consequently, the possibility of

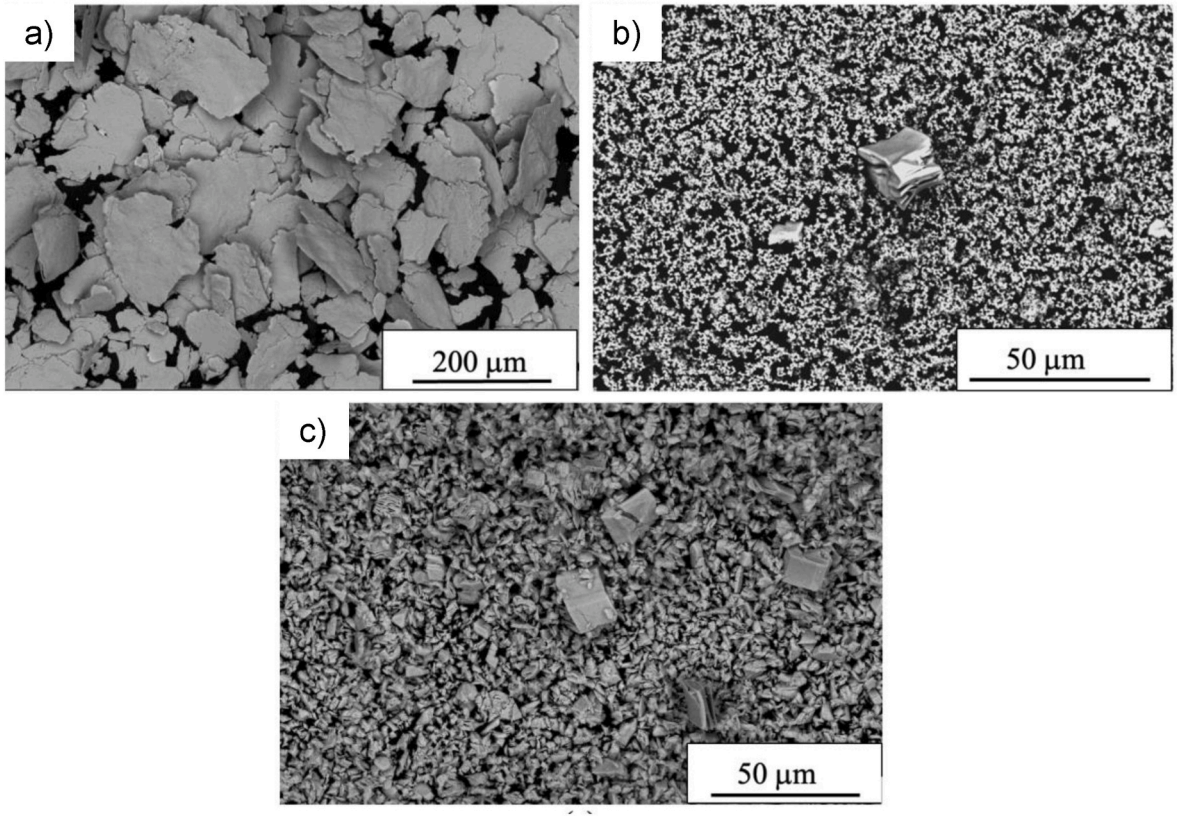

Fig. 5. SEM images of raw material powder of a) Cu, b) Ni, and c) Y_2O_3.

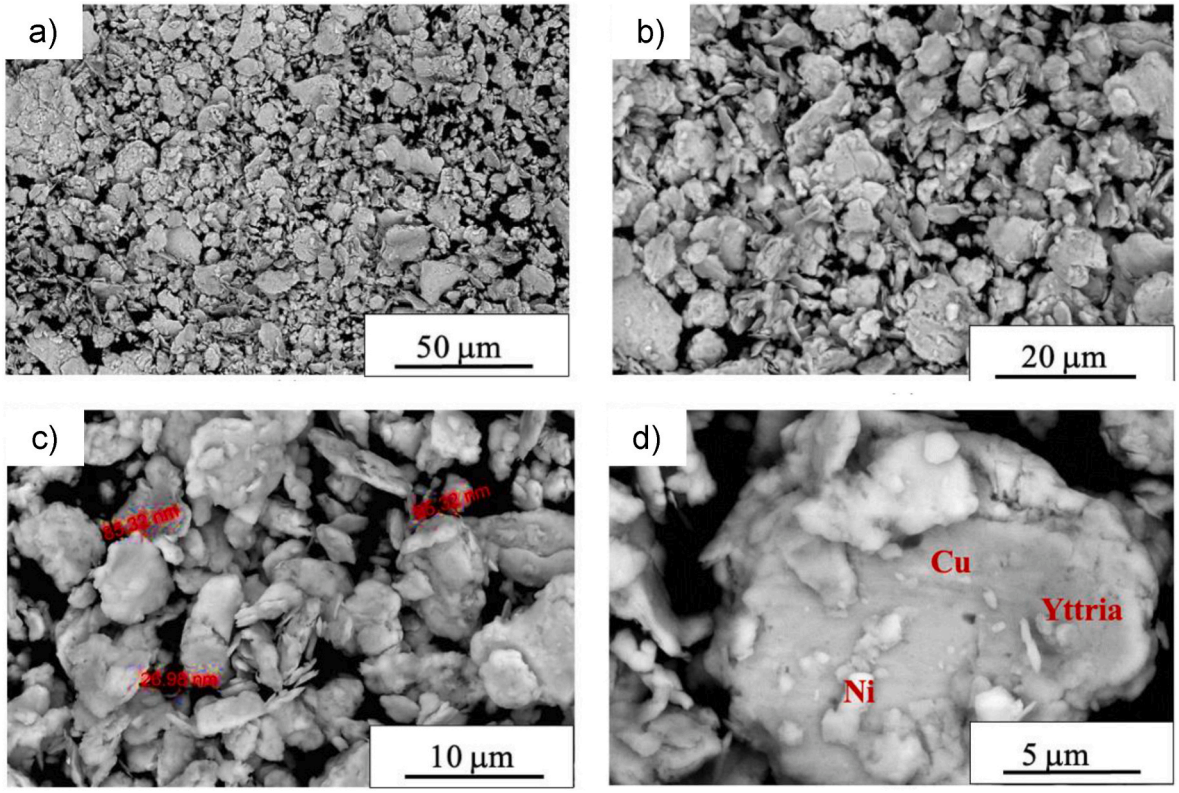

Fig. 6. SEM images of raw powder of Cu–Ni-1 wt.% Y_2O_3 after milling at different magnifications.

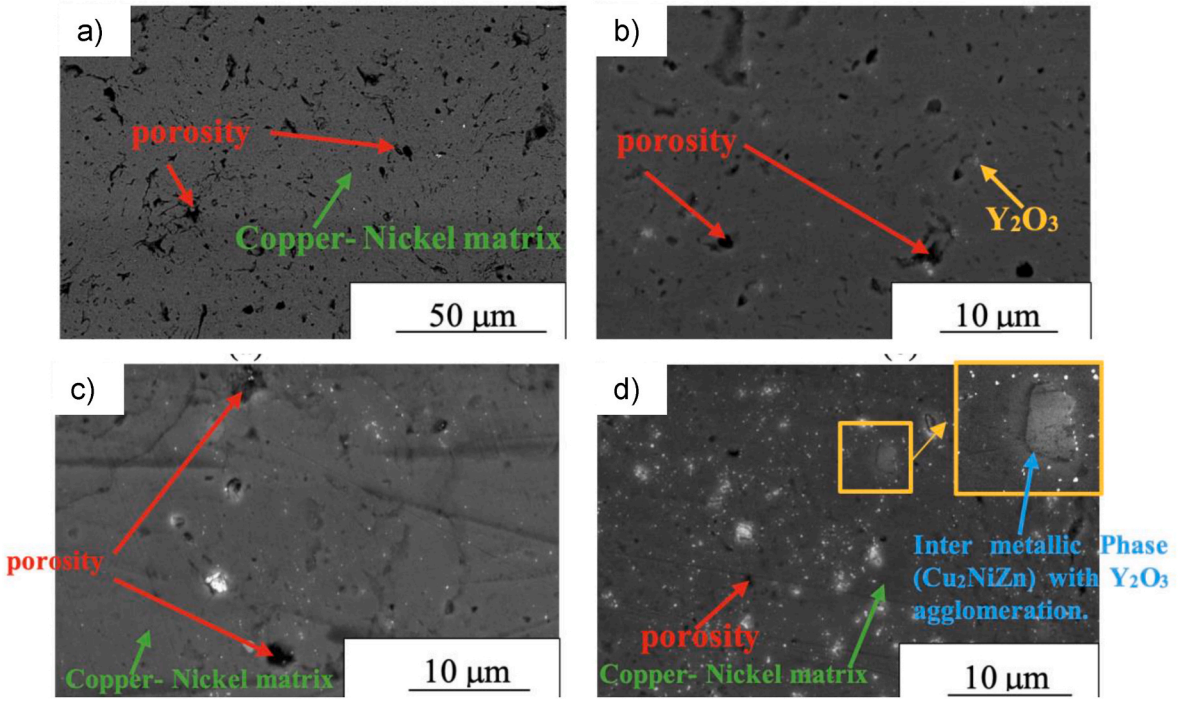

Fig. 7. SEM images of the Cu–Ni sintered composites with different content of Y_2O_3 (a) 0 wt%, (b) 0.5 wt%, (c) 1 wt%, and (d) 1.5 wt%, with the formation of (Cu_2NiZn) intermetallic phase during sintering as the Cu–Ni matrix comprises trace amount of brass. Agglomeration of Y_2O_3 particles is pronounced in Cu–Ni composite reinforced with 1.5 wt% Y_2O_3.

forming interfacial bonds by interacting with electrons from a stable ceramic compound like Y_2O_3 is limited, thus hindering effective load transfer. Here, the establishment of a solid interface between the Cu matrix and the reinforcements is primarily considered mechanical. During the sintering process, which combines pressure and elevated temperatures, close atomic-scale contact occurs between mating surfaces, enabling diffusion and the formation of a strong interface [35,36]. This intimate contact leads to a well-defined interface, enhancing

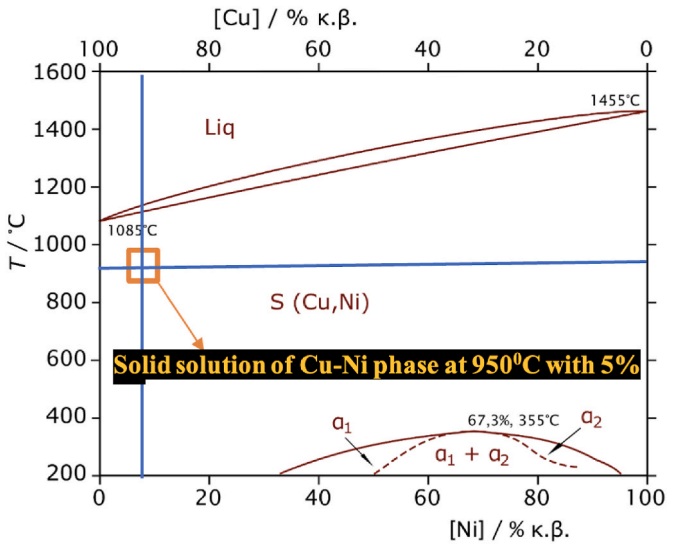

Fig. 8. Phase diagram of the Cu–Ni binary system showing the formation of Cu–Ni solid solution for 5 wt% Ni at the sintering temperature of 950 °C [28].

composite properties.

The EDX analysis and elemental mapping for 1 wt% Y_2O_3 sample are illustrated in Fig. 10. This specimen was chosen for EDX as well as for mapping analysis because it possesses the highest density, as will be detailed in the subsequent section. The EDX analysis of the sintered specimen confirms the existence of Cu, Ni, Zn, Yttrium (Y), and O. Thus, the EDX results represent the elemental structure of the specimens which confirm that the specimen is free from any undesirable phases. The elemental mapping confirms the uniformity of the consolidated microstructure. It is shown that the main spectra contain exclusively five principal components including Cu, Ni, Zn, Y, and O as emphasised in the EDX analysis. No other elements or oxides were detected, proving the effectiveness of the manufacturing process. Additionally, the mapping clarifies a highly homogeneous distribution of the applied element powders within the microstructure. It is reported that the homogeneous distribution of reinforcements in the sintered composite can positively affect the mechanical and physical properties [37–39].

3.2. Density measurements

The bulk density of parts manufactured through PM is a well-known factor significantly influencing their mechanical performance. Table 3 presents the data of the theoretical, experimental, and relative densities of Cu–Ni nanocomposites with added Y_2O_3. The relative density for pure Cu–Ni and the current nanocomposites, including Cu–Ni/(0.5) Y_2O_3, Cu–Ni/(1) Y_2O_3, and Cu–Ni/(1.5) Y_2O_3, are determined as follows: 89%, 81%, 85%, and 82%, respectively.

In comparison, Stobrawa and Rdzawski [24] reported a relative density of 87% for Cu-1 wt.% Y_2O_3 produced via the PM technique, achieved with an applied pressure. This value is consistent with that obtained in this study for Cu–Ni/(1) Y_2O_3, which recorded 85% at a pressure of 400 MPa and a pressure of 650 MPa. Table 3 also demonstrates that as the relative density decreases in sintered composites, the percentage of porosity increases. However, among all Cu–Ni/Y_2O_3 composites, 0.5 wt% Y_2O_3 exhibits the highest porosity. This is primarily attributed to the challenges of achieving good wettability and dispersion of the Y_2O_3 reinforcement within the Cu–Ni matrix. These difficulties in reinforcement distribution led to reduced mechanical, electrical, and thermal properties in Cu-MMCs strengthened with ceramics [24].

3.3. Mechanical properties

3.3.1. Hardness

Hardness measurements were employed to assess the strengthening

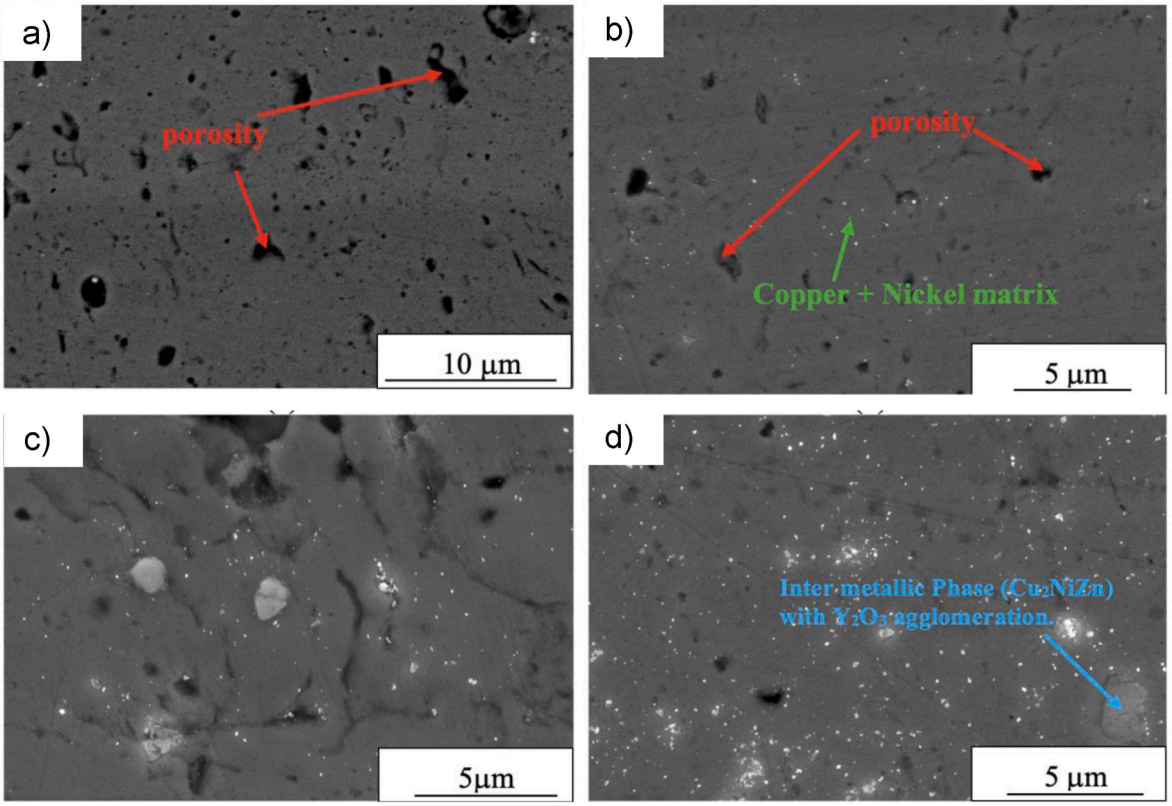

Fig. 9. High magnification SEM images of the sintered Cu–Ni composites with different wt.% of Y_2O_3 (a) 0 wt%, (b) 0.5 wt%, (c) 1 wt%, (d) 1.5 wt%.

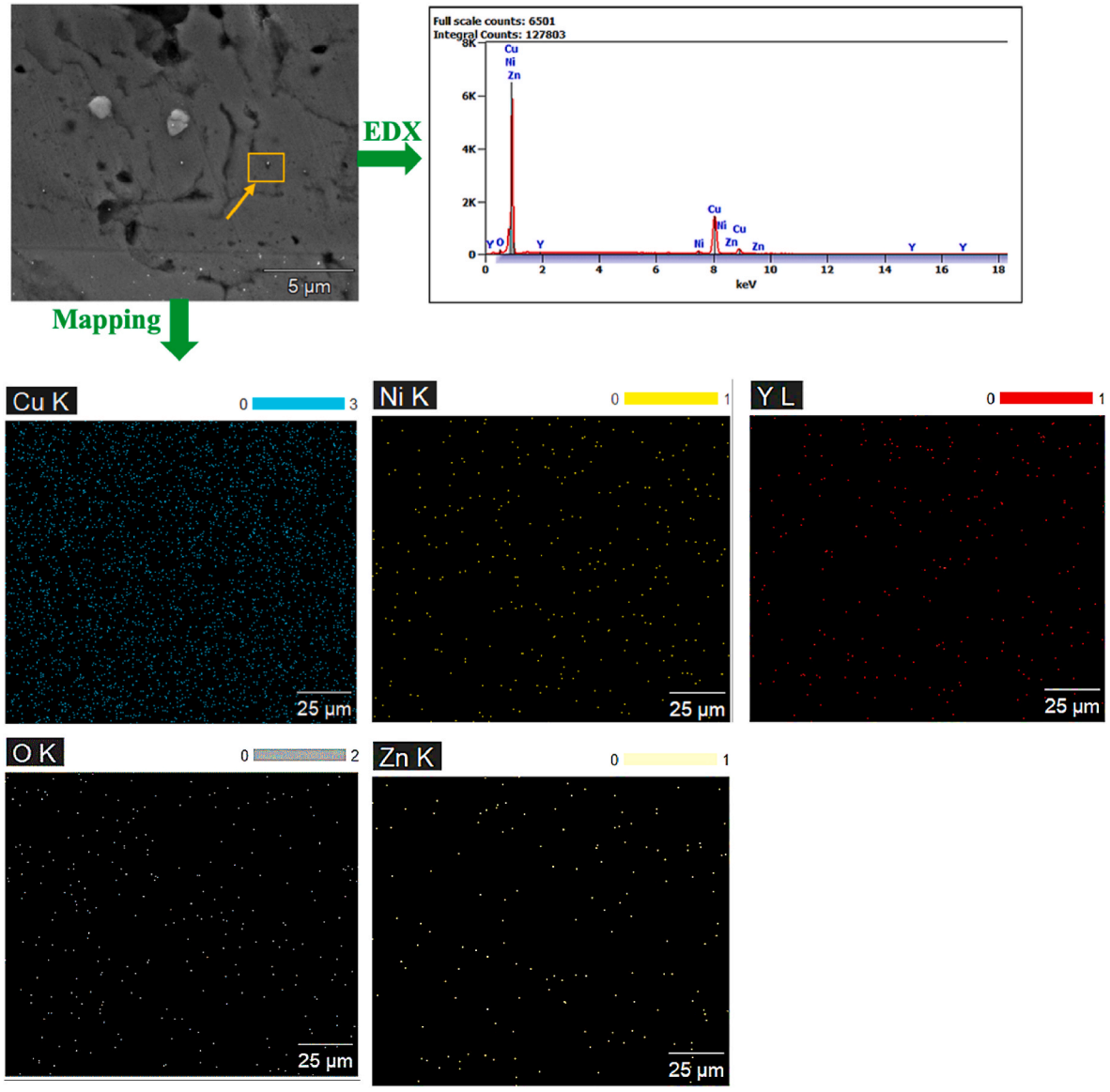

Fig. 10. EDX analysis of the region containing a nanoparticle and elemental mapping in the sample of Cu–Ni composite containing 1 wt% Y_2O_3.

Table 3
Density data for Cu–Ni composites with Y_2O_3 additions: A summary of theoretical, experimental, and relative densities for Cu–Ni nanocomposites featuring different Y_2O_3 contents, highlighting the impact of Y_2O_3 on relative density and porosity.

Condition	Density (g/cm^3)		Relative Density (%)	Porosity, %
	Theoretical	Experimental		
Cu–Ni	8.957	7.96 ±0.5	89	11
Cu–Ni/0.5% Y_2O_3	8.92	7.20 ±0.7	81	19
Cu–Ni/1% Y_2O_3	8.887	7.55 ±0.6	85	15
Cu–Ni/1.5% Y_2O_3	8.852	7.26 ±0.7	82	18

impact of Y_2O_3 and Ni particles as reinforcement materials and to identify surface imperfections. The macro-hardness values of the polished surfaces of the Cu–Ni/Y_2O_3 composites were determined by taking an average of three readings across each specimen's surface using the vickers macro hardness test. Fig. 11 present the hardness values for the various studied conditions. The findings reveal that the hardness values show a gradual increase with the rising Y_2O_3 content, peaking at 1% Y_2O_3. The macro hardness rises from 51 HV for Cu–Ni to 84 HV for Cu–Ni/(1) Y_2O_3, achieving a 1.65 enhancement factor, and then reduced to 69 HV for 1.5 wt% of Y_2O_3.

It is apparent that Cu-1 wt.% Y_2O_3 composites exhibit the highest hardness values among all the studied conditions. This result can be attributed not only to the reinforcing effect of Y_2O_3 but also to their high density and minimal porosity content. For further illustration, previous investigations have shown that good dispersion of nanoparticles in the Cu matrix leads to ceramic particulates stabilizing around grain boundaries. These particulates serve as effective barriers to dislocation movement within the matrix, leading to enhanced resistance to indentation and thus higher hardness [40,41]. For composites with a fraction higher than 1 wt% of Y_2O_3, hardness is decreased due to the high agglomeration of ceramic Y_2O_3 particles in the Cu matrix, which results in the formation of pores within the final composites as reported by Stobrawa et Rdzawski [24]. The reduction in hardness can also be attributed to the formation of the (Cu_2NiZn) intermetallic phase during sintering. The precipitation of semi-coherent (Cu2NiZn) particles can lead to an age-softening effect [42], allowing dislocations to bypass

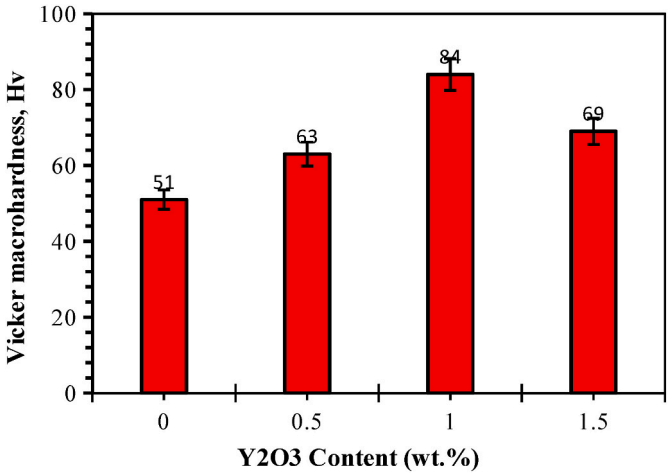

Fig. 11. The effect of Y_2O_3 content on macro-hardness of Cu–Ni nanocomposite. The composite Cu–Ni/(1) Y_2O_3 showed the highest hardness, compared to pure Cu–Ni, and the composites with 0.5 and 1.5 wt% Y_2O_3.

these secondary phase regions. This facilitates slip and reduces the composites' resistance to permanent deformation, decreasing hardness.

Geng et al. [23] found that increasing Y_2O_3 up to 2.0 wt% increases hardness from 35.5 to 42.9 HB with the addition of Y_2O_3 due to fine grain strengthening under Y_2O_3 distribution at the grain boundaries. They reported that Y_2O_3 particles gather to the grain boundaries so that they hinder the Cu grain from growing freely to a certain extent, causing Cu grain refining, which means an increase in strength and hardness. Additionally, Okazaki et al. [18] utilized the powder metallurgy method to produce Cu–Ni–Ag/Y_2O_3 composites. Their findings showed a peak hardness of 210 MPa for the composition containing 5% Y_2O_3 and 5% nickel. Additionally, Salur et al. [41] reported a pronounced enhancement in hardness of 7075 Al-alloy by 164 % due to addition of 0.5 wt% Y_2O_3-nanoparticles via powder metallurgy route. Overall, Cu–Ni/(1) Y_2O_3 exhibited the greatest hardness, showing a 64.7% enhancement compared to pure Cu–Ni and surpassing other composites containing 0.5 and 1.5 wt% of Y_2O_3.

3.3.2. Compression strength

A compressive test was performed on the sintered Cu–Ni and Cu–Ni/Y_2O_3 nanocomposites, and their strengths were compared. Fig. 12 displays the engineering stress-strain curves for the Cu–Ni/Y_2O_3 nanocomposites with varying Y_2O_3 content. It is observed that the Cu–Ni/(1) Y_2O_3 displays greater ductility compared to the pure form and other Y_2O_3 ratios. Additionally, specimens of 0, 1, and 1.5 wt% of Y_2O_3 showed yield strength of about 320, 340 and 360 MPa, respectively. It is clear that the 1.5% Y_2O_3 composition exhibited the highest yield strength, exceeding 360 MPa. These findings highlight the enhancement of mechanical properties in Cu–Ni/Y_2O_3 nanocomposites compared to pure Cu–Ni. This improvement in mechanical properties can be attributed to the dispersion hardening effect resulting from the uniform distribution of hard reinforcements in the metal matrix [43,44]. As previously mentioned, dispersion hardening involves the incorporation of small, hard particles into the metal, which hinders dislocation movement and consequently enhances the material's strength properties.

Specimen 1 wt% Y_2O_3 exhibited the highest density and hardness values among the studied conditions. However, its yield strength was lower than the 1.5 wt% Y_2O_3 specimen. Interestingly, the 1 wt% Y_2O_3 specimen showed the highest ductility. The high ductility may be attributed not only to the lower reinforcement percentage, but also to the high wettability that occurred in this specimen. According to Li et al. [45], The enhanced ductility observed in the sintered composites can be attributed to their increased capacity to sustain plastic strain. The

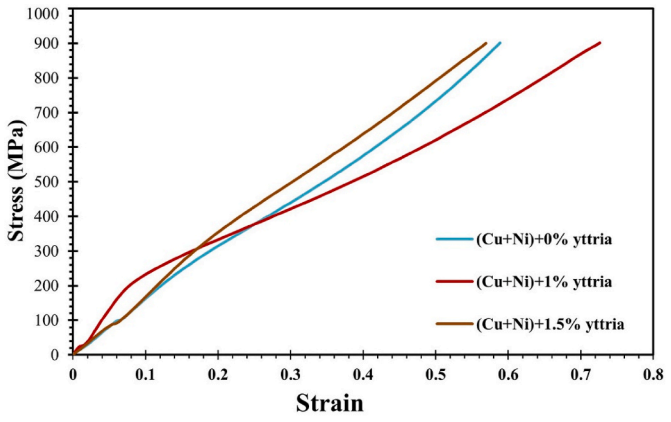

Fig. 12. Sstress-strain curve of the sintered Cu–Ni composites with different contents of Y_2O_3.

combination of hardness and ductility in the 1 wt% specimen demonstrates that multiple factors beyond just reinforcement content, including interfacial reactions and wetting behavior, influence the final mechanical properties of the composites.

3.4. Mechanical properties

3.4.1. Electrical conductivity

The Electrical conductivity of a material describes its ability to conduct electrical current and so it presents a free charge of electrons or ions inside the material. Our composite consists of a Cu matrix, and metals are good conductors, but ceramic reinforcement (such as Y_2O_3 particles) hinders the motion of free electrons. Resistivity measurements were converted to electrical conductivity, presented as a percentage of the International Annealed Cu Standard (IACS%), following ASTM standard B 193-72. Fig. 13 displays that the electrical conductivity of the composites decreased with addition of 0.5 wt% Y_2O_3, then significantly increased at 1 wt% and 1.5 wt% Y_2O_3. The initial reduction in conductivity with 0.5% Y_2O_3 can be attributed to the presence of the ceramic Y_2O_3 particles at grain boundaries impeding electron movement in the conductive Cu matrix, as explained by Geng et al. [23]. Further, Y_2O_3 itself has no electrical conductivity, so its presence retards electron motion. Besides, decreasing the conductivity at 0.5 wt% Y_2O_3 likely due to higher porosity and agglomeration effects. However, the subsequent increase in conductivity at 1 wt% and 1.5 wt% Y_2O_3 despite higher reinforcement content, indicates additional factors at play. The higher density and lower porosity of the 1 wt% and 1.5 wt% specimens likely

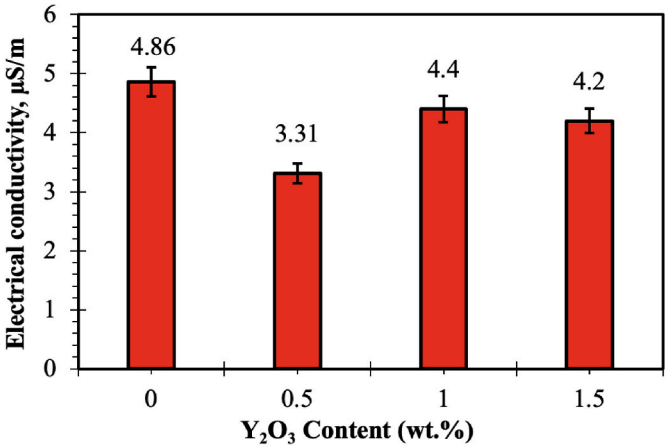

Fig. 13. The Electrical conductivity of the sintered Cu–Ni composites with different wt.% of Y_2O_3.

enabled better distribution and less agglomeration of the Y_2O_3 particles, reducing interruption of electron flow. Therefore, while Y_2O_3 addition decreases conductivity compared to pure Cu by impeding electron motion, improved distribution, and density at 1 wt% Y_2O_3 likely enabled the highest conductivity between the composites, making it a suitable composition for thermal and electronic applications.

3.4.2. Thermal conductivity

Thermal conductivity (λ) is an inherent property of a material that characterizes its capacity to conduct heat. Heat conduction takes place in the direction of decreasing temperature because higher temperatures correspond to greater molecular energy or increased molecular motion. When adjacent molecules collide, energy is transferred from the more energetic ones to those with lower energy levels. The electrical and thermal conductivities are related to the Wiedemann Franz Law depending on Lorentz number L, absolute temperature T, and electrical resistivity ρ, which can be stated as λ=(L•T)/ρ. Fig. 14 show the fluctuation in thermal conductivity of the investigated composite materials. The addition of Y_2O_3 particles to the Cu matrix led to a decrease in the thermal conductivity of Cu at 0.5 wt% Y_2O_3. This lowered thermal conductivity suggests significant resistance to heat transfer. The low thermal conductivity can be attributed to two factors: (1)The inherently low thermal conductivity of Y_2O_3 particles (about 14 W/m.k). (2)The separation between Cu and Y_2O_3 particles, with the Y_2O_3 particles surrounded by cavities. This leads to poor chemical affinity or wettability between the Cu and Y_2O_3. As a result, creating a good bonding between the matrix and reinforcement with both high mechanical strength and low thermal resistance is challenging.

For composites with more than 0.5 wt% Y_2O_3, the thermal conductivity increases again and becomes higher for the composite with 1 wt% Y_2O_3. It then slightly decreases for 1.5% Y_2O_3, likely due to high agglomeration and porosity. The presence of pores causes a decline in thermal conductivity, as the conductivity of pores is zero.

The material densification, quantity, and interface condition of the particles play a key role in thermal conductivity [46]. In Cu– Y_2O_3 nanocomposites, heat transfer is influenced by free electrons in the Cu matrix and photons in Y2O3 particles. The interface between them can scatter this movement. Thus, the thermal conduction in the Cu–Ni/Y_2O_3 nanocomposite hinges on the Cu matrix, Y_2O_3 particles, and their joint interface. The smooth interface between Cu and Y_2O_3 nanoparticles, devoid of reactants, can promote efficient heat transfer.

3.4.3. Coefficient of thermal expansion

The CTE is a fundamental property that characterizes how a material's dimensions change with temperature variations. In the case of our Cu–5%Ni composites with varying weight percentages (wt.%) of Y_2O_3, CTE plays a pivotal role in understanding their response to temperature changes. Fig. 15 presents the CTE variations of these composites, which were examined in an open-air environment across a temperature range from 100 °C to 700 °C. The Cu–Ni matrix without any Y_2O_3 content exhibits the highest CTE of $50x10^{-6}$ K^{-1} at 700 °C. This is a characteristic of metals like Cu and Ni, which typically exhibit significant expansion when subjected to elevated temperatures. However, as Y_2O_3 nanoparticles are introduced into the matrix, a notable decrease in CTE is observed. This reduction in CTE can be attributed to a combination of factors. First, the increased porosity resulting from the lower density of Y_2O_3 particles contributes to the improved thermal expansion coefficient. Moreover, the interface formed between the Y_2O_3 reinforcement, and the matrix serves as a constraint, effectively limiting the overall thermal expansion of the matrix itself, as discussed previously [47]. Remarkably, at 700 °C the sample containing 0.5 wt% Y_2O_3 exhibits CTE value of 40×10^{-6} $°C^{-1}$ which corresponds to a 20% reduction compared to the Cu–Ni matrix, demonstrating the efficacy of Y_2O_3 in constraining thermal expansion. Furthermore, the 1 wt% Y_2O_3 sample records a strong reduction in CTE value reaching 4.5×10^{-6} $°C^{-1}$, which resembles 90% reduction with respect to that of Cu–Ni matrix. Despite the higher Y_2O_3 content in the 1.5 wt% sample, the 1 wt% Y_2O_3 matrix achieves the lowest CTE value, while the 1.5 wt% Y_2O_3 composite displays 40×10^{-6} $°C^{-1}$ (40 % reduction) compared to the Cu–Ni matrix. This remarkable reduction in CTE in the Cu–Ni composite with 1 wt% Y_2O_3 can be attributed to several contributing factors. These include improved bonding between the Cu–Ni matrix and Y_2O_3 particles, higher density, and reduced agglomeration of Y_2O_3 within the matrix. Consequently, this composite composition, featuring 1 wt% Y_2O_3, appears to be particularly well-suited for high-temperature applications. The CTE of metal-matrix composites is a multifaceted property influenced by various factors, such as the type, morphology, and volume fraction of reinforcements, the microstructure of the matrix, thermal history, and the presence and extent of porosity. Additionally, internal stresses generated at the interface between the matrix and reinforcement can significantly affect the material's thermal expansion behavior [48]. Orowan strengthening, a phenomenon observed when dislocations are hindered by the presence of fine and high-melting-point particles [49,50], also plays a role. Furthermore, during the cooling of the composite material from the sintering temperature, thermal stresses arise due to the distinct thermal expansion coefficients of the different elements in the Cu–Ni matrix and Y_2O_3 reinforcements. This leads to the formation of a high-density dislocation zone, but the ceramic particles like Y_2O_3 are too hard to be accommodated by these dislocations. Consequently, when dislocations encounter these hard particles within the Cu–Ni-based composite, they tend to obstruct and bend around them,

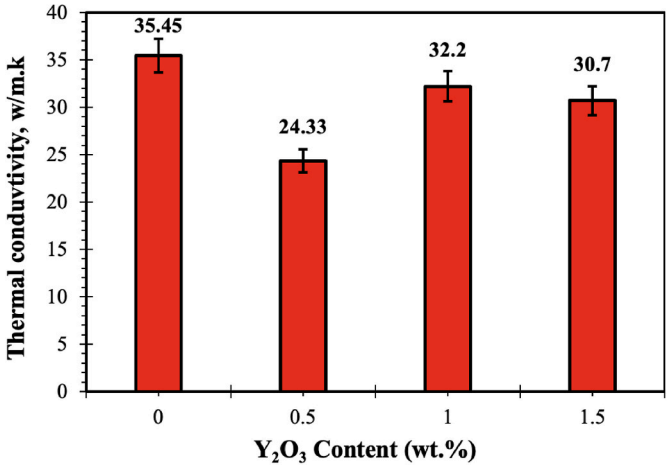

Fig. 14. The thermal conductivity of the sintered Cu–Ni composites with different wt.% of Y_2O_3.

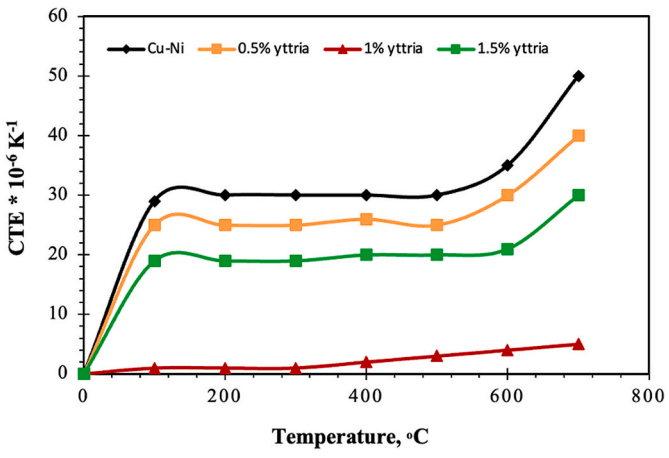

Fig. 15. Coefficient of thermal expansion behavior of the sintered Cu–Ni composites with different wt.% contents of Y_2O_3.

creating loops around the ceramic particles. This behavior effectively restricts the movement of dislocations within the material [47]. Additionally, the significant disparity in the coefficient of thermal expansion (CTE) between Cu ($\sim 17 \times 10^{-6}\ ^{\circ}C^{-1}$) and Y_2O_3 reinforcements ($\sim 6–7 \times 10^{-6}\ ^{\circ}C^{-1}$) results in the formation of a plastic zone with a high dislocation density near the reinforcements within the Cu–Ni matrix. This plastic zone contributes to the enhancement of the composite's strength properties [51]. This study provides valuable insights into tailoring the properties of Cu–Ni nanocomposites for diverse engineering applications. Further research could explore the optimization of processing parameters to enhance the performance of these composites materials even further.

4. Conclusions

In this study, we investigated the microstructural, mechanical, thermal, and electrical properties of Cu–Ni composites (5 wt% Ni) reinforced with varying contents of Y_2O_3. (0, 0.5, 1, and 1.5 wt%). The key findings and conclusions are as follows:

1. The microstructural analyses using XRD and SEM revealed the occurrence of the Cu–Ni/Y_2O_3 composites with tailored fractions of Y_2O_3. The Cu–Ni/Y_2O_3 composites displayed the presence of pores, with the 0.5 wt% Y_2O_3 composite showing the highest porosity. This was attributed to challenges in achieving good wettability and dispersion of Y_2O_3 in the Cu-5wt.%Ni matrix.
2. The relative density of the composites decreased with increasing Y_2O_3 content. For instance, the relative density of Cu–Ni/1 wt%Y_2O_3 was 85%, while pure Cu–Ni composite exhibited a relative density of 89%.
3. Macro-hardness values showed a gradual increase with rising the Y_2O_3 content, peaking at 1 wt% Y_2O_3, which is attributed to both the reinforcing effect of Y_2O_3 and to the attainable high density. Similarly, compressive tests indicated improved ductility in Cu-5wt.%Ni/1wt. Y_2O_3 compared to Cu-5wt.%Ni. The 1.5 wt% Y_2O_3 composite exhibited the highest yield strength of around 360 MPa.
4. Electrical conductivity initially decreased with 0.5 wt% Y_2O_3 addition due to interruption of electron flow. However, it relatively increased at 1 wt% and 1.5 wt% Y_2O_3 due to the improved Y_2O_3 distribution and densification.
5. Thermal conductivity decreased with 0.5 wt% Y_2O_3, while it increased again with higher Y_2O_3 content, peaking at 1 wt% Y_2O_3, and then slightly decreased at 1.5 wt% Y_2O_3 due to agglomeration and porosity.
6. Coefficient of Thermal Expansion (CTE) decreased as Y_2O_3 content increased, with the 1 wt% Y_2O_3 composite displaying the lowest CTE. Improved bonding between the matrix and Y_2O_3 particles, higher density, and reduced agglomeration contributed to the lower CTE.

Declaration of competing interest

The authors declare that they have no known competing financial interests or personal relationships that could have appeared to influence the work reported in this paper.

Acknowledgements

W. A. would like to acknowledge the Technology Innovation Commercialization Office (TICO) at Zagazig University in Egypt for supporting this project.

References

[1] Qin J, Wu Y, Yu M, Liu B, Liu H, Weiss K-P, Li L, Li H, Niu E, Bruzzone P. Manufacture of ITER feeder sample conductors. Fusion Eng Des 2013;88:1461–4. https://doi.org/10.1016/j.fusengdes.2013.01.008.

[2] Paton NE. Materials for advanced space propulsion systems. Mater Sci Eng 1991; 143:21–9. https://doi.org/10.1016/0921-5093(91)90722-Y.

[3] Hamid FS, El-Kady OAE, Essa ARS, El-Nikhaily AEG, Elsayed A, Abd-Elaziem W. Synthesis and characterization of titanium carbide and/or alumina nanoparticle reinforced copper matrix composites by spark plasma sintering. J Mater Eng Perform 2022;31:5583–92. https://doi.org/10.1007/s11665-022-06639-1.

[4] Shabadi R, Avettand-Fènoël MN, Simar A, Taillard R, Jain PK, Johnson R. Thermal conductivity in yttria dispersed copper. Mater Des 2015;65:869–77. https://doi.org/10.1016/j.matdes.2014.09.083.

[5] Hamid ZA, Moustafa SF, Morsy FA, Khalifa NAA, Mouez FA. Fabrication and characterization copper/diamond composites for heat sink application using powder metallurgy. Nat Sci 2011;3:936–47. https://doi.org/10.4236/ns.2011.311120.

[6] Yehia HM, Nouh F, El-Kady OA, Abd-Elaziem W, Elsayed Em. Studying the microstructure, electrical, and electrochemical behaviour of the Cu-10WC/x GNs for electrochemical machining electrode and energy application. Int J Mach Mach Mater 2022;24:430–52. https://doi.org/10.1504/IJMMM.2022.128461.

[7] Abd-Elaziem W, Liu J, Ghoniem N, Li X. Effect of nanoparticles on creep behaviour of metals: a review. J Mater Res Technol 2023;26:3025–53. https://doi.org/10.1016/j.jmrt.2023.08.068.

[8] Froes FH. The structural applications of mechanical alloying. JOM 1990;42:24–5. https://doi.org/10.1007/BF03220464.

[9] Biswas K, He J, Blum ID, Wu C-I, Hogan TP, Seidman DN, Dravid VP, Kanatzidis MG. High-performance bulk thermoelectrics with all-scale hierarchical architectures. Nature 2012;489:414–8. https://doi.org/10.1038/nature11439.

[10] Abd-Elaziem W, Khedr M, Abd-Elaziem A-E, Allah MMA, Mousa AA, Yehia HM, Daoush WM, El-Baky MAA. Particle-reinforced polymer matrix composites (PMC) fabricated by 3D printing. J Inorg Organomet Polym 2023. https://doi.org/10.1007/s10904-023-02819-1.

[11] Synthesis and Characterization of Hybrid Fiber-Reinforced Polymer by Adding Ceramic Nanoparticles for Aeronautical Structural Applications, (n.d.). https://www.mdpi.com/2073-4360/13/23/4116 (accessed September 13, 2023).

[12] Liu Y, Liu Y, Wang B, Qiu J, Liu B, Tang H. Microstructures evolution and mechanical properties of a powder metallurgical titanium alloy with Yttrium addition. Mater Manuf Process 2010;25:735–9. https://doi.org/10.1080/10426910903365778.

[13] Groza JR, Gibeling JC. Principles of particle selection for dispersion-strengthened copper. Mater Sci Eng 1993;171:115–25. https://doi.org/10.1016/0921-5093(93)90398-X.

[14] Rajkovic V, Bozic D, Jovanovic MT. Properties of copper matrix reinforced with various size and amount of Al2O3 particles. J Mater Process Technol 2008;200: 106–14. https://doi.org/10.1016/j.jmatprotec.2007.08.019.

[15] Humphreys FJ, Ardakani MG. Grain boundary migration and Zener pinning in particle-containing copper crystals. Acta Mater 1996;44:2717–27. https://doi.org/10.1016/1359-6454(95)00421-1.

[16] Akramifard HR, Shamanian M, Sabbaghian M, Esmailzadeh M. Microstructure and mechanical properties of Cu/SiC metal matrix composite fabricated via friction stir processing. Mater Des 2014;54:838–44. https://doi.org/10.1016/j.matdes.2013.08.107.

[17] R. Singh, Thermal control of high-powered desktop and laptop microprocessors using two-phase and single-phase loop cooling systems, (n.d.)..

[18] Okazaki AK, Martins MVS, Carvalhal M, Monteiro WA, Carrió JAG. Mechanical and structural characterization of Cu-Ni-Ag/Y2O3 composites obtained by powder metallurgy. Mater Sci Forum 2012;727–728:314–9. https://doi.org/10.4028/www.scientific.net/MSF.727-728.314.

[19] El-Katatny SM, Nassef AE, El-Domiaty A, El-Garaihy WH. Fundamental analysis of cold die compaction of reinforced aluminum powder. Int. J. Eng. Tech. Res 2015;3: 180–4.

[20] Singh R, Akbarzadeh A, Mochizuki M. Sintered porous heat sink for cooling of high-powered microprocessors for server applications. Int J Heat Mass Tran 2009; 52:2289–99. https://doi.org/10.1016/j.ijheatmasstransfer.2008.11.016.

[21] Optimizing the Powder Metallurgy Parameters to Enhance the Mechanical Properties of Al-4Cu/xAl2O3 Composites Using Machine Learning and Response Surface Approaches, (n.d.). https://www.mdpi.com/2076-3417/13/13/7483 (accessed September 13, 2023).

[22] Joshi PB, Rehani B, Naik P, Patel S, Khanna PK. Studies on copper-yttria nanocomposites: high-energy ball milling versus chemical reduction method. J Nanosci Nanotechnol 2012;12:2591–7. https://doi.org/10.1166/jnn.2012.5748.

[23] Mu Z, Geng H-R, Li M-M, Nie G-L, Leng J-F. Effects of Y2O3 on the property of copper based contact materials. Compos B Eng 2013;52:51–5. https://doi.org/10.1016/j.compositesb.2013.02.036.

[24] J P S, Rdzawski Z. Dispersion - strengthened nanocrystalline copper. Journal of Achievements in Materials and Manufacturing Engineering 2007;24.

[25] Liao HT, Le MT. Optimization on selective fiber laser sintering of metallic powder. Adv Mater Res 2012;472:2519–30.

[26] Haque R, Sekh M, Kibria G, Haidar S. IMPROVEMENT OF SURFACE QUALITY OF Ti-6Al-4V ALLOY BY POWDER MIXED ELECTRICAL DISCHARGE MACHINING USING COPPER POWDER. Facta Univ – Ser Mech Eng 2023;21:63–79. https://doi.org/10.22190/FUME201215042H.

[27] Rubat du Merac M. Transparent ceramics: materials, processing, properties and applications. In: Pomeroy M, editor. Encyclopedia of materials: technical ceramics and glasses. Oxford: Elsevier; 2021. p. 399–423. https://doi.org/10.1016/B978-0-12-818542-1.00029-1.

[28] Wang CP, Liu XJ, Jiang M, Ohnuma I, Kainuma R, Ishida K. Thermodynamic database of the phase diagrams in copper base alloy systems. J Phys Chem Solid 2005;66:256–60. https://doi.org/10.1016/j.jpcs.2004.08.037.

[29] Camra J, Bielańska E, Bernasik A, Kowalski K, Zimowska M, Białas A, Najbar M. Role of Al segregation and high affinity to oxygen in formation of adhesive alumina layers on FeCr alloy support. Catal Today 2005;105:629–33. https://doi.org/10.1016/j.cattod.2005.06.015.
[30] Zhao Y, Zhang T, Chen L, Yu T, Sun J, Guan C. Microstructure and mechanical properties of Ti–C–TiN-reinforced Ni204-based laser-cladding composite coating. Ceram Int 2021;47:5918–28. https://doi.org/10.1016/j.ceramint.2020.11.054.
[31] Tharanikumar L, Mohan B, Anbuchezhiyan G. Enhancing the microstructure and mechanical properties of Si3N4–BN strengthened Al–Zn–Mg alloy hybrid nano composites using vacuum assisted stir casting method. J Mater Res Technol 2022; 20:3646–55. https://doi.org/10.1016/j.jmrt.2022.08.093.
[32] Abd-Elaziem W, Elkatatny S, Abd-Elaziem A-E, Khedr M, Abd El-baky MA, Hassan MA, Abu-Okail M, Mohammed M, Järvenpää A, Allam T, Hamada A. On the current research progress of metallic materials fabricated by laser powder bed fusion process: a review. J Mater Res Technol 2022;20:681–707. https://doi.org/10.1016/j.jmrt.2022.07.085.
[33] Singh K, Khanna V, Chaudhary V. Effect of hybrid reinforcements on the mechanical properties of copper nanocomposites. ECS J. Solid State Sci. Technol. 2022;11:097001. https://doi.org/10.1149/2162-8777/ac8bf9.
[34] Lathashankar B, Tejaswini GC, Suresh R, Swamy NHS. Advancements in diffusion bonding of aluminium and its alloys: a comprehensive review of similar and dissimilar joints. Advances in Materials and Processing Technologies 2022;8: 4659–77. https://doi.org/10.1080/2374068X.2022.2079274.
[35] Li W, Liang Y, Bai Y, Lin T, Li B, Feng J. Cu–Cu low-temperature diffusion bonding by spark plasma sintering: void closure mechanism and mechanical properties. J Mater Sci Technol 2023;139:210–23. https://doi.org/10.1016/j.jmst.2022.08.031.
[36] Zhou Y, Wang Z, Zhao J, Jiang F. Effect of ultrasonic amplitude on interfacial characteristics and mechanical properties of Ti/Al laminated metal composites fabricated by ultrasonic additive manufacturing. Addit Manuf 2023;74:103725. https://doi.org/10.1016/j.addma.2023.103725.
[37] Gao X, Yue H, Guo E, Zhang H, Lin X, Yao L, Wang B. Mechanical properties and thermal conductivity of graphene reinforced copper matrix composites. Powder Technol 2016;301:601–7. https://doi.org/10.1016/j.powtec.2016.06.045.
[38] Umasankar V, Anthony Xavior M, Karthikeyan S. Experimental evaluation of the influence of processing parameters on the mechanical properties of SiC particle reinforced AA6061 aluminium alloy matrix composite by powder processing. J Alloys Compd 2014;582:380–6. https://doi.org/10.1016/j.jallcom.2013.07.129.
[39] Microwave and spark plasma sintering of carbon nanotube and graphene reinforced aluminum matrix composite | SpringerLink, (n.d.). https://link.springer.com/article/10.1016/j.acme.2018.02.006 (accessed September 15, 2023).
[40] Groza JR, Shackelford JF. Materials processing handbook. CRC Press; 2007.
[41] Salur E, Aslan A, Kuntoğlu M, Acarer M. Effect of ball milling time on the structural characteristics and mechanical properties of nano-sized Y2O3 particle reinforced aluminum matrix composites produced by powder metallurgy route. Adv Powder Technol 2021;32:3826–44. https://doi.org/10.1016/j.apt.2021.08.031.
[42] Xu DK, Wang BJ, Li CQ, Zu TT, Han EH. Effect of icosahedral phase on the thermal stability and ageing response of a duplex structured Mg–Li alloy. Mater Des 2015; 69:124–9. https://doi.org/10.1016/j.matdes.2014.12.057.
[43] Hemanth J. Development and property evaluation of aluminum alloy reinforced with nano-ZrO2 metal matrix composites (NMMCs). Mater Sci Eng 2009;507: 110–3. https://doi.org/10.1016/j.msea.2008.11.039.
[44] Yang K, Li W, Niu P, Yang X, Xu Y. Cold sprayed AA2024/Al2O3 metal matrix composites improved by friction stir processing: microstructure characterization, mechanical performance and strengthening mechanisms. J Alloys Compd 2018; 736:115–23. https://doi.org/10.1016/j.jallcom.2017.11.132.
[45] Li J, Zhang H, Zhang Y, Che Z, Wang X. Microstructure and thermal conductivity of Cu/diamond composites with Ti-coated diamond particles produced by gas pressure infiltration. J Alloys Compd 2015;647:941–6. https://doi.org/10.1016/j.jallcom.2015.06.062.
[46] Chu K, Guo H, Jia C, Yin F, Zhang X, Liang X, Chen H. Thermal properties of carbon nanotube–copper composites for thermal management applications. Nanoscale Res Lett 2010;5:868. https://doi.org/10.1007/s11671-010-9577-2.
[47] Pan Y, Xiao S, Lu X, Zhou C, Li Y, Liu Z, Liu B, Xu W, Jia C, Qu X. Fabrication, mechanical properties and electrical conductivity of Al2O3 reinforced Cu/CNTs composites. J Alloys Compd 2019;782:1015–23. https://doi.org/10.1016/j.jallcom.2018.12.222.
[48] Li J, Whittaker M. Intermetallics: applications. In: Caballero FG, editor. Encyclopedia of materials: metals and alloys. Oxford: Elsevier; 2022. p. 339–49. https://doi.org/10.1016/B978-0-12-819726-4.00041-7.
[49] Asgharzadeh H, Eslami S. Effect of reduced graphene oxide nanoplatelets content on the mechanical and electrical properties of copper matrix composite. J Alloys Compd 2019;806:553–65. https://doi.org/10.1016/j.jallcom.2019.07.183.
[50] Geng R, Qiu F, Jiang Q-C. Reinforcement in Al matrix composites: a review of strengthening behavior of nano-sized particles. Adv Eng Mater 2018;20:1701089. https://doi.org/10.1002/adem.201701089.
[51] Aminorroaya S, Ranjbar A, Cho Y-H, Liu HK, Dahle AK. Hydrogen storage properties of Mg-10 wt% Ni alloy co-catalysed with niobium and multi-walled carbon nanotubes. Int J Hydrogen Energy 2011;36:571–9. https://doi.org/10.1016/j.ijhydene.2010.08.103.